Modulational instability of nonlinear spin waves in easy-axis antiferromagnetic chains. II. Influence of sample shape on intrinsic localized modes and dynamic spin defects

L. Q. English, M. Sato, and A. J. Sievers
Laboratory of Atomic and Solid State Physics, Cornell University, Ithaca, New York 14853-2501
(Received 26 July 2002; published 6 January 2003)

An indirect method of producing intrinsic localized modes (ILM's) is to drive an unstable uniform mode to large amplitude. In this investigation the intimate connection between the shape-dependent demagnetization factor, the modulation instability, and ILM behavior is established. The stability of the antiferromagnetic resonance (AFMR) against breakup into such ILM's is shown to depend strongly on the frequency difference between the linear AFMR and the long-wavelength limit of the spin-wave dispersion curve. This difference, which stems from the long-range dipole-dipole interactions, depends on the demagnetization factor and hence the sample shape. Here it is demonstrated initially with linear perturbation analysis and later with molecular-dynamics simulations that the instability characteristics and ILM production properties depend strongly on the sign and magnitude of the frequency difference. The simulations show that when the AFMR frequency is coincident with the spin-wave band, a spatially coherent train of ILM's appears, but this coherence is lost at long times. When the AFMR frequency is inside the spin-wave band, the Suhl instability populates the degenerate spin waves, whose subsequent modulational instability leads to traveling and decelerating ILM's. When the AFMR frequency is below the spin-wave band, a large-amplitude threshold for the instability appears. Above this threshold ILM's and localized dynamic spin flops occur, confined to specific lattice regions.

DOI: 10.1103/PhysRevB.67.024403 PACS number(s): 75.10.Hk, 75.50.Ee, 75.30.Ds, 45.05.+x

I. INTRODUCTION

A wide variety of periodic, nonlinear systems can support spatially localized excitations in addition to plane-wave ones.[1–5] Such intrinsic localized modes (ILM's) involve only a few sites in perfectly periodic lattices, are nonintegrable, and hence are outside the bounds of standard soliton theory.[6–8] For condensed-matter atomic lattices such ILM's should occur on the nanoscale but how best to produce and detect these individual ILM's is still under investigation. Present efforts focus on an indirect method, which involves the modulational instability of the large-amplitude, nonlinear uniform mode against breakup into such excitations.[5,9–14]

In magnetism the modulation instability of a homogeneous large-amplitude spin-wave mode has a long history[15] and it is usually referred to as the second-order Suhl instability.[16–18] In high power ferromagnetic resonance the uniform mode is made unstable against the exponential growth of modulational sidebands, when driven to large enough amplitude;[19,20] however, because of the small ratio of the magnetic-resonance frequency to the spin-wave bandwidth the activation of this instability does produce long-wavelength envelope solitons, but not ILM's. Recent numerical[21,22] and experimental[23–25] studies have shown that antiferromagnets provide a natural habitat for ILM's, because of their relatively large antiferromagnetic-resonance (AFMR) frequency, which essentially involves the geometric mean of the anisotropy and exchange fields. So far the analytical and numerical studies of instabilities in antiferromagnets have focused on the particular case where the uniform mode is coincident with the bottom of the spin-wave branch. This study is described in Refs. 21 and 26, hereafter referred to as (I). The inclusion of dipole-induced fields not only gives rise to an effective on-site spin anisotropy term but can also shift the frequency of the uniform mode with respect to the rest of the spin-wave spectrum.[27–29] Since the dipole-dipole interaction between spins generates a shape-dependent demagnetization field that can only modify the AFMR frequency, an effective spectral gap in the linear dispersion curve opens up at the zone center. This feature should play an important role in the modulational instability and hence in the ultimate production properties of ILM's.

In this paper the intimate connection between the shape-dependent demagnetization factor, the modulational instability, and ILM behavior is established. To isolate this connection, the same one-dimensional (1D) antiferromagnetic spin chain model described in (I) is considered, but now the shape dependence is included. The relative frequency position of the uniform mode and the long-wavelength spin waves traveling along the chain are varied by means of the sample demagnetization field. The stability analysis for the resulting uniaxial antiferromagnet is examined, and then these analytical results are compared with molecular-dynamics (MD) simulation results. In this way it is possible to explore how the sample shape influences the modulational instability process, while at the same time exploring numerically how the details of the short-time instability predictions impact the emergence of ILM's at longer times.

The next section presents the modulational stability analysis of the uniform mode in the presence of a demagnetization field. The detailed equations are given in the Appendix. In Sec. III, the analytical results are discussed and compared to numerical MD simulations. Since only the demagnetization part of the dipole-dipole field is considered in this 1D model, it is possible to shift the uniform mode above or below the dispersion curve and hence characterize all relative positions that can arise in a three-dimensional crystal.[25] The differ-

ences in the modulational instability characteristics of the three cases for the short-time scale are compared to the long-time evolution of ILM's. Three fundamentally different cases are identified: quasiperiodic ILM's occur for no gap, traveling ILM's that decelerate occur when the uniform mode is inside the linear spin-wave spectrum, and finally catastrophic ILM production occurs when there is a spectral gap. The conclusions are given in Sec. IV.

II. INSTABILITY OF THE UNIFORM MODE

A. Analysis

The modulational instability of the uniform mode for an antiferromagnetic chain with easy-axis anisotropy has been investigated in Ref. 21. It is instructive to build on that study and to examine how the addition of the demagnetizing field alters the nonlinear dynamics. Rather than consider the full expression for the dipole-dipole interaction, only the part that makes a finite sample different from an infinite one is introduced below. To simplify the analysis further only ellipsoidal sample shapes with the symmetry axis parallel to the easy axis will be considered so that the two spin-wave branches remain degenerate.

The simplest model Hamiltonian for such an antiferromagnetic spin chain, which includes information about sample shape, is

$$H=2J\sum_n \mathbf{S}_n\cdot\mathbf{S}_{n+1}-D\sum_n (S_n^z)^2 - \frac{1}{2}\frac{(g\mu_B)^2}{V}\sum_{n,n'}\mathbf{S}_n\cdot\vec{\vec{N}}\cdot\mathbf{S}_{n'}, \tag{1}$$

where $\mathbf{S}_n$ is the dimensionless classical spin vector on site n, J is the antiferromagnetic exchange constant, D the single-ion uniaxial anisotropy constant, g the spectroscopic slitting factor, μ_B the Bohr magneton, V the sample volume, and $\vec{\vec{N}}$ denotes the demagnetization tensor. Here both D and J are positive and

$$\vec{\vec{N}}=\begin{pmatrix} N_\perp & & 0 \\ & N_\perp & \\ 0 & & N_z \end{pmatrix}-\frac{4\pi}{3}\vec{\vec{I}}, \tag{2}$$

where the demagnetization factors $N_\perp$, N_z satisfy the added constraint $2N_\perp+N_z=4\pi$, and depend on the shape of the crystal.

For this classical system, each spin moves in the effective magnetic field produced by its two neighbors, the on-site anisotropy and the sample shape. The effective magnetic field at lattice site n is

$$\gamma\mathbf{H}_n^{\text{eff}}=-2\frac{J}{\hbar}(\mathbf{S}_{n-1}+\mathbf{S}_{n+1})+2\frac{D}{\hbar}S_n^z\hat{\mathbf{z}}-\frac{M_0\gamma}{S}\vec{\vec{N}}\cdot\langle\mathbf{S}\rangle, \tag{3}$$

where M_0 is the sublattice magnetization and γ is the gyromagnetic ratio. Here

$$\langle\mathbf{S}\rangle=\frac{1}{N_s}\sum_m \mathbf{S}_m,$$

where the index m goes over both sublattices. Note that in equilibrium at $T=0$ K, $\langle\mathbf{S}\rangle=0$.

In this form, the respective roles of the on-site and demagnetization terms become more apparent. Whereas the on-site field at site n depends only on the spin at that site, the demagnetization field at site n depends on the average over all spins. Thus, the Hamiltonian, given by Eq. (1), incorporates both wavelength limits of the anisotropic interaction. The dynamics is given by the torque equation

$$\frac{d\mathbf{S}_n}{dt}=\gamma\mathbf{S}_n\times\mathbf{H}_n^{\text{eff}}. \tag{4}$$

With circularly polarized variables, $s_n^{\pm}=(S_n^x\pm iS_n^y)/S$, the equation of motion for the nth site becomes

$$i\frac{ds_n^+}{dt}=-2\frac{JS}{\hbar}[(s_{n-1}^z+s_{n+1}^z)s_n^+-(s_{n-1}^++s_{n+1}^+)s_n^z] +2\frac{DS}{\hbar}s_n^zs_n^+ +\gamma M_0(N_\perp-4\pi/3)s_n^z\langle s^+\rangle -\gamma M_0(N_z-4\pi/3)s_n^+\langle s^z\rangle. \tag{5}$$

The first of the last two terms in Eq. (5) describes the dynamic demagnetization effect that gives rise to the frequency gap between the uniform mode and long-wavelength spin waves. Only for the uniform mode is this term different from zero. In contrast, the last term in Eq. (5) has an equal effect on all modes, because the average is over the z components. Its contribution appears at large amplitudes.

Here the focus in on the stability of the nonlinear uniform mode, and the details of the analytical perturbation analysis are presented in the Appendix. The uniform mode frequency is given by Eq. (A4). The perturbation variables, which measure the deviation of the spin system from the uniform mode, are introduced in Eq. (A7), then a linearized system of evolution equations for these perturbation variables is obtained, see Eq. (A10). The precise form of $\vec{\vec{T}}$, the Jacobian matrix whose eigenvalues determine the stability of the uniform mode, is given in Eqs. (A11) and (A12). Due to the presence of the demagnetization field, $\vec{\vec{T}}$ depends on a dimensionless sample-shape parameter defined as

$$\beta\equiv(g\mu_BM_0/4JS)(N_\perp-4\pi/3), \tag{6}$$

which measures the ratio of the demagnetization energy to the exchange energy.

The eigenvalues $t_{(n)}$ of $\vec{\vec{T}}$ determine the stability of the uniform mode. We define the stability coefficients $\lambda_{(n)}$ as

$$2JS[i\lambda_{(n)}]\equiv it_{(n)}. \tag{7}$$

The stability of the uniform mode requires the imaginary parts of all $\lambda_{(n)}$ to vanish. With the stability parameter associated with the most unstable eigenvalue identified as λ, solving Eq. (A14) gives the solution for λ, Eq. (A15).

B. MD simulations

To make contact with the analytical predictions at short times as well as to examine the longer-time dynamics of the nonlinear system after ILM formation, MD simulations are used. For this purpose, the classical dynamics of a chain of 1024 spins is simulated, using the Runge-Kutta algorithm (fourth order) to numerically solve the equations of motion. The initial configuration of the spins is that of a uniform mode of amplitude f. This means that the two sublattices are given transverse amplitudes of f and $-\alpha f$, respectively. A small-amplitude noise field (0.004% of the exchange field) is added at each iteration (256 times per uniform mode period) to simulate the effects of random spin fluctuations. This noise is important in that it seeds the instability process; the noise level fixes the initial amplitudes of the $q \neq 0$ spin-wave modes. A small Landau-Lifshitz damping term[20] is incorporated in the simulations to stabilize the MD simulation results. The accuracy of the constraint of constant spin length is checked after each iteration and found to be on the order of 10^{-7}. Periodic boundary conditions are used throughout. Much of the analysis requires reciprocal space information, which is extracted by using the fast Fourier-transform algorithm on the discrete spin-site data.

III. ANALYTICAL RESULTS AND COMPARISON WITH MD SIMULATIONS

A. Initial modulational instability and the frequency gap

1. No spectral gap ($\beta = 0$)

This case represents a uniform mode, which lies on the spin-wave dispersion curve and has been discussed in (I). Here the intent is to present real and imaginary parts of the stability coefficient λ, defined in Eq. (7) to establish the connection with the frequency gap cases to be considered subsequently. MD simulations are used both to confirm the linear stability analysis at short times and also to show the departure of the system from the predictions of the perturbation analysis at times close to ILM formation.

The main features of the instability for $\beta = 0$ are highlighted in Fig. 1(a), where λ is plotted as a function of wave vector for various amplitudes f. The linear case ($f^2 \ll 1$) is the dashed curve, and reproduces the linear spin-wave dispersion curve. Note that the linear AFMR frequency is subtracted off in this representation since λ measures a frequency relative to that of the uniform mode. As f increases, all plane-wave modes shift to lower frequencies relative to the uniform mode, and at long wavelengths, λ becomes imaginary. The imaginary part of λ, represented by the dotted curves, identifies the important modulational wave vectors associated with the instability. λ vanishes as $Q \to 0$ in accord with Eq. (A18), and it attains its maximum value at a wave number that increases monotonically with the uniform mode amplitude f.

Figure 1(b) depicts the spatial Fourier spectrum of the transverse spin component from an MD simulation at two different times before the emergence of ILM's. The initial uniform mode amplitude $f = 0.2$ and the wave number of maximum growth is found to be $Q_{\max} = 0.085 q_{BZ}$. For $f = 0.1$ (not shown), $Q_{\max} = 0.041 q_{BZ}$. Both values are in good agreement with the analytical prediction [see Fig. 1(a)]. An additional feature in Fig. 1(b), beyond linear stability analysis, is the emergence of peaks at $\pm 2\, Q_{\max}$ at times close to the appearance of ILM's (dotted line). At this point the system has diverged from the analytical predictions.

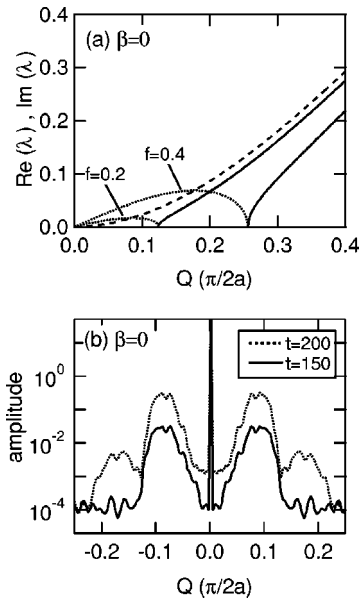

FIG. 1. (a) The real and imaginary parts of the stability coefficient λ versus modulation wave vector Q for $\beta = 0$. The real part represents the frequency of spin waves minus the AFMR frequency, and the imaginary part gives the growth rate. The figure shows three values for the uniform mode amplitude f. The dashed trace is the linear dispersion curve. The other traces correspond to $f = 0.2$ and 0.4. The imaginary part of λ is represented by dotted lines, and the real part by solid lines. (b) Modulation amplitude versus wave vector. MD simulation results for a chain of 1024 spins. A uniform mode with $f = 0.2$ is excited at $t = 0$. The plots show the spatial Fourier components at times $t = 150$ and 200 AFMR periods (solid and dotted lines, respectively). Sidebands at a characteristic wave number emerge (note the logarithmic y axis).

Plotting the logarithmic amplitude of the fastest growing spin wave as a function of time for $f = 0.1$ and 0.2 reveals that the growth is indeed exponential at early times and the growth rate increases with increasing f, in accord with the analytical result. Again, at times close to the emergence of ILM's, the exponential growth of the modulation saturates.

2. Spectral gap ($\beta < 0$)

The uniform mode is now shifted to lower frequencies relative to the spin waves, see Eqs. (A5) and (A6). Thus, effectively there is a discontinuity in the dispersion curve at $q = 0$. This regime characterizes a flat platelike sample.

Figure 2(a) presents the real and imaginary parts of λ, the stability parameter, plotted versus the wave number for $\beta = -0.2$. Shown is the small-amplitude dispersion curve (dashed line) associated with the linear spin waves and also the modulation curves for three different amplitudes f of the uniform mode. Subsequently these modulations on the excited uniform mode will be called nonlinear spin waves.

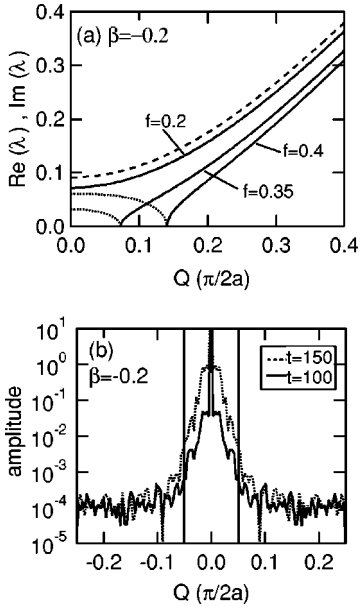

FIG. 2. (a) The real and imaginary parts of λ versus modulation wave vector Q for $\beta=-0.2$. The spin-wave dispersion curves in the presence of a demagnetization field are displayed for four values of the AFMR amplitude f. The linear dispersion curve (dashed line) has a gap at $Q=0$, which decreases as f increases ($f=0.2$). The stability coefficient becomes imaginary for some Q (dotted lines) at $f=0.35$ and 0.40. In contrast to Fig. 1(a), now the imaginary parts extend all the way to $Q=0$. (b) Modulation amplitude versus wave vector at times $t=100$ (solid line) and $t=150$ periods (dotted line) for $f=0.34$. The cutoff wave number is $Q=0.051$, in good agreement with the analytical prediction from (a) (vertical lines).

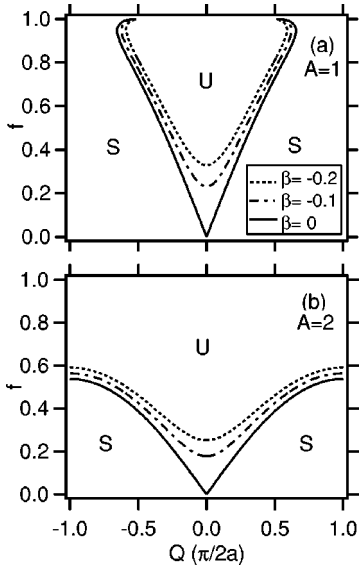

FIG. 3. Regions of modulational instability for the uniform mode in the (f,Q) plane when $\beta\leqslant 0$. The labels S and U identify stable and unstable regions in parameter space. (a) The anisotropy parameter $A=1$. Solid line, $\beta=0$; dot-dashed line, $\beta=-0.1$, and dotted line, $\beta=-0.2$. As β becomes negative the uniform mode for sufficiently small amplitude becomes stable to all Q. The large Q region is always stable regardless of the spin-wave amplitude. (b) The anisotropy parameter $A=2$. Now the uniform mode with large amplitude becomes unstable to perturbations of any wave vector.

There are several clear differences in the figure when compared to the $\beta=0$ cases shown in Fig. 1. Now there is a discontinuity in the linear dispersion curve at $Q=0$, signified by $\lambda(Q\rightarrow 0)>0$. As f increases, the frequency difference between the nonlinear spin waves and the uniform mode decreases (solid curves), until at the critical amplitude $f_{\rm crit}$, the lowest nonlinear spin-wave frequency becomes coincident with the uniform mode. Here the real part of λ vanishes, the imaginary part appears (dotted curve), and an instability develops. In the range $0\leqslant f<f_{\rm crit}$, the frequencies of all spin waves remain real and the uniform mode is stable.

The Q dependence of the growth rate [Im(λ)], shown by the dotted curves in Fig. 2(a) for $f>f_{\rm crit}$, is quite different from the $\beta=0$ cases. Contrary to $\beta=0$ where the growth rate is sharply peaked at a particular nonzero wave number, a fairly flat Q dependence appears extending all the way to $Q=0$. For f sufficiently large, only a shallow peak emerges at nonzero Q on this broad background.

The spatial Fourier components of the MD simulation for this case are shown in Fig. 2(b) for two times prior to the development of spatial localization ($t=100$ and 150). Here time is measured in units of $T_{\rm AFMR}$ for the case $\beta=0$. The distribution of spin waves is seen to extend from $Q=0$ to a cutoff $Q_c(f)$ consistent with the analytical result (marked in the figure with vertical lines).

In order to produce a modulational instability it is necessary to overcome the frequency gap created by the demagnetization field and this depends on the amplitude. Figure 3 quantifies this statement, by demonstrating exactly where a gap in the stability region of the (f,Q) plane appears as β becomes negative. In this figure the lines separating regions of stability and instability are displayed. These lines are defined by the equation $\lambda(f,Q)=0$. Shown in the figure are the instability regions for $\beta=0$ (solid line), -0.1 (dot-dashed line), and -0.2 (dotted line). For both values $A=1$ [Fig. 3(a)] and 2 [Fig. 3(b)] of the dimensionless anisotropy parameter, the region of instability shrinks as β is decreased from zero. For sufficiently small f and any A the uniform mode is stable for all modulation wave vectors. For $A=1$, we see an instability "bubble" centered at $Q=0$ for all β, whereas for $A=2$, a uniform mode of sufficient amplitude becomes unstable to all wave numbers Q.

Figure 4 shows the amplitude threshold for the instability $f_{\rm crit}$, as a function of the demagnetization factor, obtained both from analytical results and MD simulations. In the simulations, the prefactor $(g\mu_B M_0/4JS)$ is set to 1 in Eq. (6). The amplitude $f_{\rm crit}$ is the smallest value for which instability occurs. Analytically it is defined by the equation $\lambda(f_{\rm crit},Q\rightarrow 0)=0$, which is solved numerically to yield $f_{\rm crit}(\beta)$. The demagnetization factor $N_\perp$ ranges from $4\pi/3$ to 0, corresponding to a sphere and a disk, respectively. The corresponding β goes from 0 to $-\frac{1}{3}$. The numerical data represented by the open circles agrees nicely with the predicted curve. The small offset is due to the inclusion of weak damping in the simulations. We see that as β decreases, the critical amplitude $f_{\rm crit}$ increases. This means that as the uniform mode moves further away from the spin-wave band (to

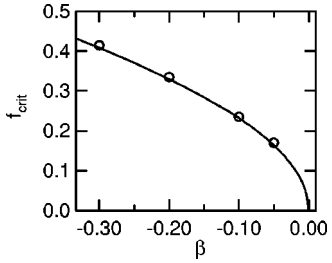

FIG. 4. The critical amplitude f_{crit} as a function of β. The prefactor in Eq. (6) is set to 1 in the MD simulations so β ranges from $-\frac{1}{3}$ to 0. The solid line identifies the analytical curve and the open circles are MD simulation results. The simulations yield slightly higher values due to the presence of weak damping.

lower frequencies) it becomes increasingly difficult to make the uniform mode unstable.

Consider the case where the uniform mode is excited to increasingly large amplitude by an external driver. The uniform mode breaks up when it reaches the threshold amplitude f_{crit} and hence saturates. The energy in the uniform mode just prior to breakup depends on the demagnetization factor ($\beta<0$), as shown in Fig. 4, hence, the smaller β, the larger the energy in the uniform mode, and the more energy that can be transferred into emerging ILM's when the instability occurs.

3. Second-order Suhl instability ($\beta>0$)

For a rod-shaped sample ($\beta>0$), the uniform mode is shifted up into the spin-wave spectrum and becomes degenerate with a subset of spin-wave modes. For the 1D case there are two isolated points at $Q=\pm q_{\mathrm{deg}}$ where this occurs. The analytical results are shown in Fig. 5(a) where the real and imaginary parts of the stability parameter λ are plotted for $\beta=0.2$. The dashed trace represents the linear dispersion curve, and the solid and dotted traces are the real and imaginary parts of λ for $f=0.4$. Note that the instability region is very asymmetric about q_{deg}, and highly oriented towards larger q values. If damping is included in the equations of motion then an amplitude threshold appears. These results illustrate the second-order Suhl instability for an antiferromagnet and extend the analysis of Ref. 18. The corresponding MD simulations shown in Fig. 5(b) demonstrate that the modulational instability does indeed populate spin waves near q_{deg}. The figure shows the Fourier transform at two times, as measured in units of T_{AFMR} for the case $\beta=0$, and $t=150$ and 300 for an initial uniform mode amplitude of $f=0.2$. By $t=300$ the amplitudes of the degenerate spin waves have grown appreciably, as evidenced by the emergence of nonlinear spatial harmonics. With continued growth these highly excited spin waves quickly become modulationally unstable themselves.

The regions of stability and instability are mapped out in Fig. 6, where the amplitude of the uniform mode is plotted versus the modulation wave number. Two values of $\beta=0.1$ (solid line) and 0.2 (dotted line) display the systematics. In Fig. 6(a), $A=1$, and in Fig. 6(b), $A=2$. For small f, the instability shrinks to two points in reciprocal space, $\pm q_{\mathrm{deg}}$.

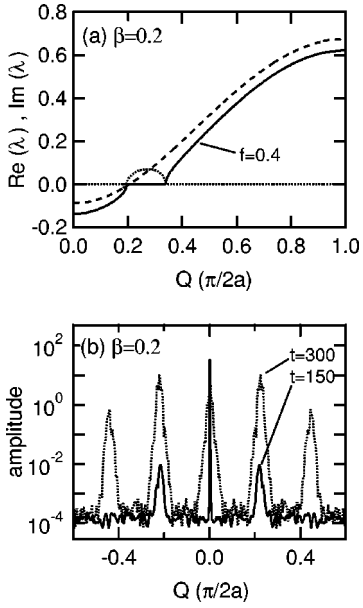

FIG. 5. (a) The real and imaginary parts of the stability coefficient λ versus modulation wave vector Q for $\beta=0.2$. The linear uniform mode is now inside the spin-wave band, as evidenced by the negative frequencies at small Q in the linear curve (dashed trace). For $f=0.4$ the imaginary part of λ is represented by dotted lines, and the real part by solid lines. (b) Modulation amplitude versus wave vector. MD simulations show the growth of spin waves that are near frequency coincidence with the AFMR. The solid and dotted traces show the spatial Fourier transform taken at $t=150$ and 300 periods, respectively.

Since q_{deg} depends on the position of the uniform mode with respect to the spin-wave band, it will also depend both on β and A, as seen in the figure. Note that for any $\beta>0$ and for both values of A, there exists a region of stability in the neighborhood of $Q=0$, separating the two instability regions. The region of instability becomes ever more asymmetric with respect to $\pm q_{\mathrm{deg}}$ as f increases.

B. Short-time pattern formation and long-time-scale ILM production signatures

1. Quasiperiodic ILM's for $\beta=0$

Figure 7 shows the time evolution of the energy at each site in the form of a density plot of spin energy (gray scale) as a function of spin site and time. Dark shades represent areas of high energy. At $t=0$ the uniform mode is excited with a specific amplitude of $f=0.2$ (uniform shading over all sites). After about $200T_{\mathrm{AFMR}}$ a regularly spaced train of incipient ILM's emerges. After some additional time, on the order of 100 periods, the spatial phase coherence of the periodic train of ILM's is lost.

The details of the modulational instability process govern the initial spacing of incipient ILM's in the lattice since the characteristic length scale of a pattern is often set by the most unstable wavelength found in the instability.[30] Figure 8(a) shows the amplitude distribution at $t=285T_{\mathrm{AFMR}}$ in the early stages of ILM formation. Here the amplitude, which shows roughly a Gaussian envelope, is plotted on a linear

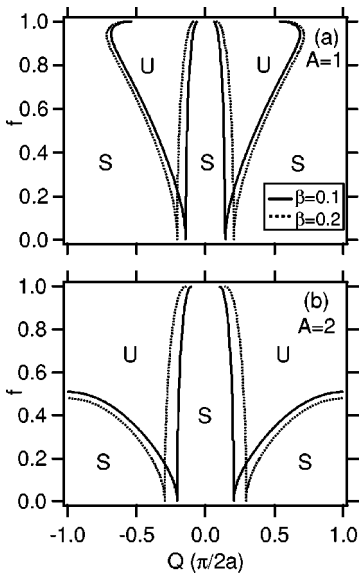

FIG. 6. Regions of modulational instability for the uniform mode in the (f,Q) plane when $\beta>0$. The labels S and U identify stable and unstable regions in parameter space. (a) The anisotropy parameter $A=1$. Solid line, $\beta=0.1$, and dotted line, $\beta=0.2$. As β becomes positive the uniform mode becomes stable at all amplitudes for small Q. However, the uniform mode even for very small amplitudes becomes unstable to a specific Q. (b) The anisotropy parameter $A=2$. The results are similar to (a).

scale. Two higher harmonic peaks can clearly be discerned. It was already shown in Fig. 1(b) that when the first spatial Fourier component had sufficient amplitude, secondary peaks at twice the predicted wave number appeared. In general spatial harmonics are generated at integer multiples of the initial wave number. These spatial harmonics continue to grow until the incipient ILM's emerge. The resulting q-space distribution represents a reciprocal lattice with spacing $Q_{\max}=0.085q_{BZ}$ in agreement with our analytical predictions.

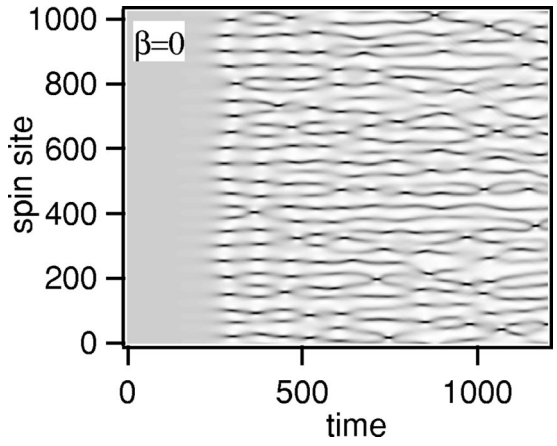

FIG. 7. Time evolution of the uniform mode energy density distribution in real space for $\beta=0$. $f=0.2$ at $t=0$. In this gray scale dark shades represent areas of high energy. The large-amplitude uniform mode is stable (uniform shading) until about at $t=200$. It then breaks up into spatially periodic ILM's but this spatial coherence is lost at long times.

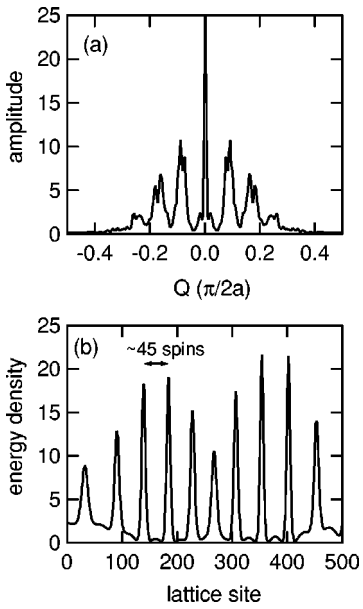

FIG. 8. (a) The Fourier spectrum of the transverse spin amplitude versus modulation wave number for $t=285$. The reciprocal lattice of ILM's with a Gaussian-like envelope is clearly visible. (b) Spin energy versus spin site revealing the periodic array of ILM's at early times.

Figure 8(b) shows the real-space picture for the same MD simulation taken at $t=285$. This lattice spacing depends on the initial amplitude of the uniform mode. In particular, for $f=0.1$ the ILM spacing is roughly twice as large as for $f=0.2$, since $Q_{\max}$ is about half as large. At these short times the analytical predictions agree with the simulation results.

2. Threshold for the creation of ILM's and localized spin flops for $\beta<0$

For the case of a frequency gap the MD simulations give rise to a catastrophic production process. Typical results are shown in Fig. 9. Again, the gray scale represents the energy plotted as a function of spin site versus time. From the random noise a single initial region of localization forms at around $t=175$ periods. The amplitude of this ILM grows very quickly, taking energy from the rest of the lattice, and then very quickly it divides into a number of strongly localized branches. For sufficiently large negative values of β, as shown here, so much energy rushes into the region occupied by the ILM that many of these branches represent localized spin flops. In this arrangement a few of the spins on one sublattice flip over into a locally canted ferromagnetic arrangement with respect to their neighbors, thus creating a dynamic point defect which is nearly stationary. Spin-wave packets are emitted to either side of these high-energy time trajectories.

To demonstrate that during the ignition process both ILM's and dynamic spin defects are produced, the z component of the spins on the large-amplitude sublattice are examined at different times. The z component of spins on the other sublattice does not change sign. Figure 10(a) illustrates that the spins in the regions of high energy (black lines in Fig. 9)

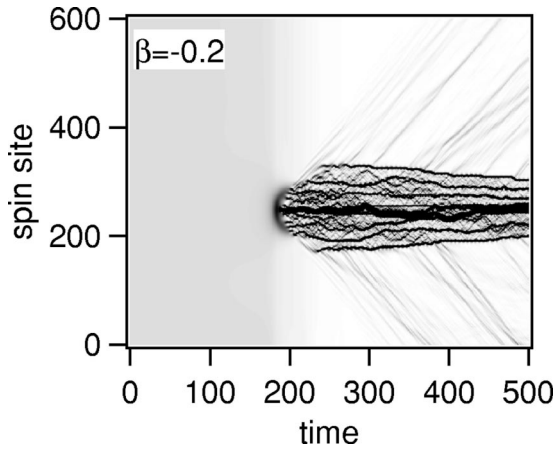

FIG. 9. Time evolution of the uniform mode energy density distribution in real space for $\beta=-0.2$. The initial AFMR amplitude is $f=0.34$, just above threshold for the $A=1$ case. In this gray scale dark shades represent areas of high energy. Initially only one broad ILM forms in the entire lattice of 1024 spins. Energy is rapidly transferred from the rest of the lattice to this region and the resultant excitation breaks up into a number of strongly localized and nearly stationary dynamic defects represented by the nearly parallel black trajectories. The fact that these trajectories converge indicates that these dynamic defects attract each other. The numerous faint lines at $\pm 45°$ indicate that spin waves are also emitted from this highly excited region.

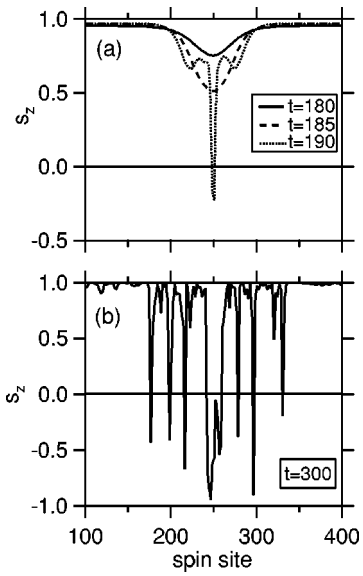

FIG. 10. Time evolution of the z component of the larger-amplitude sublattice near the time of localization for the case of an energy gap. (a) The z component of the larger-amplitude sublattice at three times: $t=180$ (solid), 185 (dashed), and 190 (dotted). Far from the excitation the z component grows with increasing time indicating smaller excitation energy here. In the excitation region, the z component decreases and the energy grows with increasing time. Finally for $t=190$ the dotted trace drops below $s_z=0$, indicating that the spin has flipped through the plane of symmetry. (b) Plot of the z components for the different lattice sites as in (a) but at $t=300$, after the creation process is completed. Now there are eight regions that have undergone spin flips. Each of the localized regions of high energy shown in Fig. 9 corresponds to a localized spin flop, which requires more energy than does an ILM.

flip through the plane of symmetry. This occurs after $t=190$ periods. Initially (at around $t=180$ periods) localization begins in one region of the spin chain as shown in Fig. 10(a). The center of the initially broad ILM grows in strength [the dashed line in Fig. 10(a)] while the wings over a large lattice region decrease. At $t=190$ periods the center continues to accumulate energy from the lattice wings, causing a few sublattice spins at the center to flip over and align parallel with their neighbors (dotted line). These neighboring spins on the other sublattice also precess at increased amplitude but never so much as to flip. A small amount of mixing between the $(+)$ and $(-)$ modes is observed. Furthermore, it is found that the transverse spin component of a given spin remains very nearly out of phase with that of its neighbors on the other sublattice, even though the phase now varies throughout a sublattice. Thus the situation can be considered the dynamic localized analog of the spin-flop transition observed in antiferromagnets when one of the uniform modes is driven to zero frequency with an applied dc magnetic field.[28,31]

Even more interesting is the slightly longer-time evolution of the z component of the sublattice spins. In Fig. 10(b) the z components are plotted for time $t=300$ periods. By now all of the strongly localized features shown in Fig. 9 are associated with a spin flop and represent a stationary point defect. With time, some of these point defects evolve back into a sharply localized ILM and the z-component spikes shrink back to positive values. However at the time shown here the central region of Fig. 10(b) represents a very large defect, encompassing many spin sites. Its energy came from the plane-wave excitations, which have now essentially disappeared. These dynamic defects appear to act as black holes.

Even for an initial uniform mode amplitude only slightly above f_{crit}, the process of localization for this case happens over a very short-time scale in a burstlike phenomenon. In reciprocal space, this burst manifests itself as a very sudden transition from the excitation of spin waves to the broad q-space distribution characteristic of ILM formation. For $\beta<0$, even at these short times the analytical results cannot predict the dramatic MD simulation findings.

3. Beyond the Suhl instability: ILM's for $\beta>0$

Exploring the intermediate- and long-time behavior of the spin system when the uniform mode is inside the spin-wave band also has produced some interesting insights. Traveling ILM-like trains can emerge from the second-order instability of coincident spin waves. A typical MD simulation for the case of a resonant interaction between the uniform mode and the spin-wave branch is shown in Fig. 11. Here $\beta=0.2$. The time evolution of the energy at each site in the form of an energy density plot (gray scale) is presented as a function of spin site versus time. A standing-wave pattern forms from the uniform mode at about 250 periods. This pattern is due to the excitation of $\pm q_{\mathrm{deg}}$. Almost immediately this is replaced by a diagonally striped pattern in Fig. 11. ILM's traveling at the group velocity emerge out of this distribution. Within a

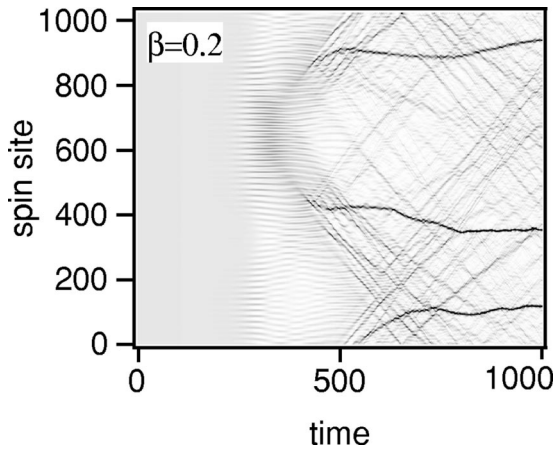

FIG. 11. Time evolution of the uniform mode energy density distribution in real space for $\beta=0.2$. The initial AFMR amplitude is $f=0.2$ for the $A=1$ case. In this gray scale dark shades represent areas of high energy. The uniform mode is stable until about $t=200$ after which it breaks up into a standing-wave pattern associated with the degenerate spin waves. This standing-wave pattern is then replaced by the diagonal stripes, due to the modulational instability of these spin waves. Traveling ILM's form, decelerate, and become large-amplitude stationary ILM's.

few 100 periods as they become strongly localized, the ILM quickly decelerate, and at long times become nearly stationary large-amplitude ILM's. This observation is consistent with the early findings from numerical studies on moving ILM's.[32] Also see Ref. 26, where the trapping of ILM's is connected to the lattice discreteness.

It is instructive to examine the double Fourier transform of the transverse spin variables over a specific time interval of Fig. 11 to follow the excitation in q space. Figure 12 shows the population of normal modes, i.e., points in (ω,q) space, as well as local modes, i.e., straight lines in (ω,q) space, for two different time windows of 200-periods width. In Fig. 12(a), the time window starts at $t=300$. Some energy remains in the uniform modes but most has been transferred to the spin excitation at $q=q_{\rm deg}$ and along the incipient tangent line to the spin-wave dispersion curve at this point. This signature in (ω,q) space is identified with the initial traveling spin-wave packets, which are evolving into moving ILM's. Our studies of such reciprocal space plots indicate that the initial traveling ILM's always avoid overlap with the spin-wave band, i.e., the tangent line is shifted with respect to the dispersion curve.

To illustrate the evolution in q space, Fig. 12(b) shows the results starting at $t=800$ periods. Here the entire normal-mode spectrum is populated and in addition, at the bottom of the spin-wave spectrum three ILM's appear. Two of these local modes are moving since the linear excitation pattern has finite slope, while the lowest-frequency ILM is stationary. All three of these line features have large localized transverse spin amplitude. The evolution of the ILM dynamics in q space is as follows: after the shifted ILM tangent line is formed at $\pm q_{\rm deg}$ then, because of the lattice discreteness, its center position moves down in frequency with the tangent line following the dispersion curve at that point. At slow

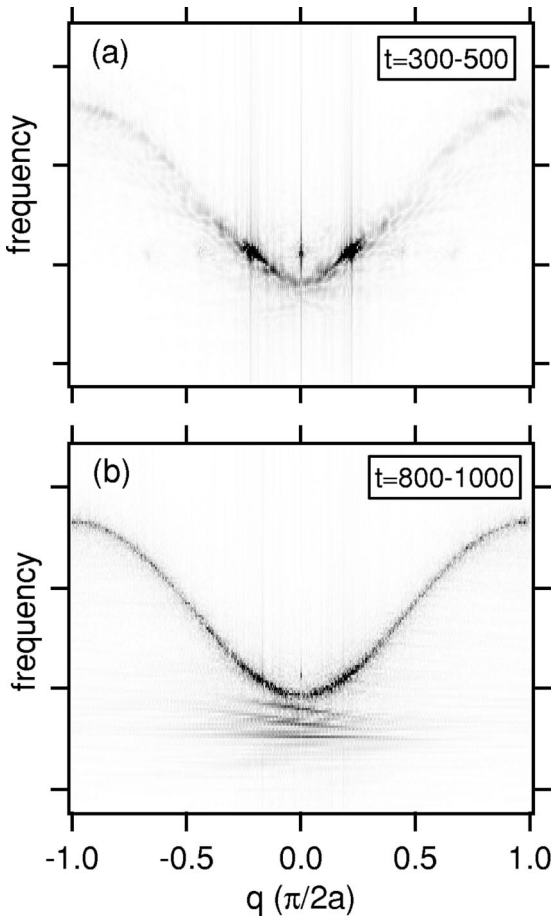

FIG. 12. Fourier-space representation (ω,q) of the time evolution of the transverse spin deviation. The parameters are the same as in Fig. 11. (a) $t=300$, $\Delta t=200$: the excitation is transferred from the uniform mode to the spin waves with the same frequency. These large-amplitude spin waves are unstable and excite resonant traveling ILM's near $\pm q_{\rm deg}$, whose signature is the density in the shifted tangent to the spin-wave band. (b) $t=800$, $\Delta t=200$: the resonant traveling ILM's at large wave vector lose energy due to the lattice discreteness and evolve into the nearly stationary ILM's with frequencies below the dispersion curve shown here.

enough speed it finally appears completely below the dispersion curve.

Now lets examine Fig. 12(a) in more detail and make the connection to the next step beyond the Suhl instability. During the first stage, the uniform mode transfers energy to the coincident spin waves at $\pm q_{\rm deg}$. Spatial harmonics appear at ± 2 and $\pm 3q_{\rm deg}$. Thus at short times, a nonlinear standing-wave pattern is created. In the second stage, ILM's emerge due to a secondary instability. In this stage, the spin waves at $\pm q_{\rm deg}$ become modulationally unstable.[21]

To isolate this second instability we examine the linear perturbation analysis of the specific case where the initial large-amplitude excitation is not at $q=0$ but instead at $q=\pm\pi/8a$. (The transfer of energy from $q=0$ to finite q is already considered to have taken place with one-half of the initial energy at each location.) Figure 13 illustrates this secondary instability, showing analytical results for the real and imaginary parts of λ, for a spin wave at $q=\pi/8a$, one of the

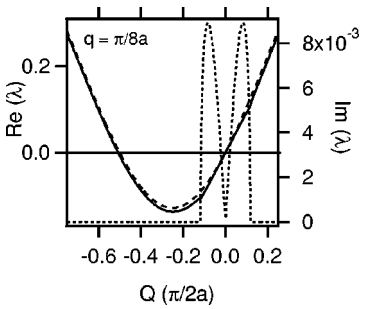

FIG. 13. The real and imaginary parts of the stability coefficient λ versus modulation wave vector for a nonlinearly excited spin wave at $q=\pi/8a$. The dashed line represents the linear dispersion curve. For the $q=\pi/8a$ spin wave of amplitude $f=0.15$ the solid and dotted traces are the real and imaginary parts of λ, respectively. Note that the solid trace is tangential to the linear dispersion curve at $q=\pi/8a$.

$q=\pm\pi/8a$ pair, each with amplitude $f=0.15$. The dashed line represents the linear dispersion curve. The solid and dotted traces identify the real and imaginary parts of the stability coefficient λ. The instability region is characterized by two peaks in the imaginary part appearing on either side of $q=\pi/8a$. This means that spin-wave modes of those two wave-number bands will rapidly grow in amplitude. Their (real) frequencies are determined by the solid line, which is tangential to the dispersion curve at $q=\pi/8a$. Thus, the original large-amplitude spin wave will become modulationally unstable against certain modes that lie on the solid line in Fig. 13.

To examine the long-time behavior of this case, a $t=0$ spin configuration with a pair of excited $q=\pm\pi/8a$ spin waves for $\beta=0$ has been used as the initial condition for the MD simulations. The results are shown in Fig. 14. Again the

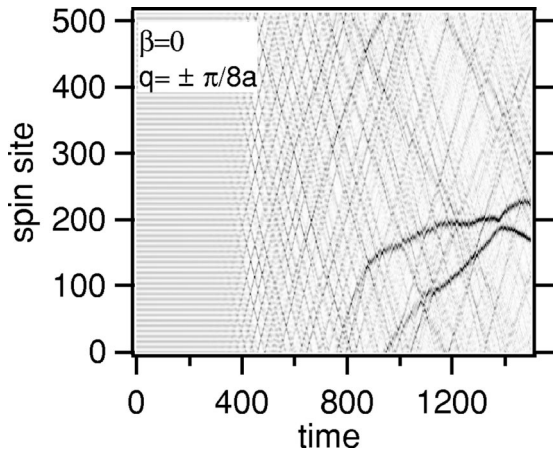

FIG. 14. Time evolution of the $q=\pm\pi/8a$ mode energy density distribution in real space for $\beta=0$. The initial amplitude of the excited pair of spin waves at $q=\pm\pi/8a$ is $f=0.15$ for the $A=1$ case. In this gray scale the dark shades represent areas of high energy. The standing-wave pattern is stable until about $t=400$. It then breaks up into the diagonal stripes indicating traveling ILM's due to the modulational instability of these spin waves. These ILM's decelerate. The dynamics is qualitatively similar to that shown in Fig. 11.

amplitude of each of the two spin waves is $f=0.15$ to correspond to the previous case in which the uniform mode was initially excited to $f=0.20$. It takes about 350 periods before the initial standing-wave configuration breaks up into moving ILM's, and these ILM's decelerate much more slowly than for the $q=0$ example shown in Fig. 11, indicating that the additional Fourier components produced in the uniform instability enhance ILM production. However, the final long-time ILM's shown in Fig. 14 have roughly the same profile as those shown in Fig. 11.

IV. CONCLUSION

The three cases ($\beta=0$, $\beta<0$, $\beta>0$) examined here initiate three distinct types of instabilities, according to the classification scheme used in the area of pattern formation.[30] The Suhl case, $\beta>0$, leads to a Type-I instability, where the instability appears at a nonzero wavelength, and then, as f is increased, a surrounding band of unstable wavelengths develops. The no gap case, $\beta=0$, exhibits a Type-II instability, characterized by the growth rate of waves peaked at a nonzero wave number, but extending down to $q=0$, where it goes to zero. Finally, the gap case, $\beta<0$, exhibits a Type-III instability, where the maximum growth rate occurs at $q=0$. These three types of instabilities are schematically represented in Fig. 7 of Ref. 30. In our model, all three of these pattern-forming instabilities can be encountered by varying the shape parameter β through zero. It should also be noted that numerical analysis on a system with biaxial on-site anisotropy, for which a perturbation analysis has not been carried out, shows qualitatively similar instability behavior. Thus the modulational instability features discussed here are not unique to the uniaxial spin system.

We have extended the modulational instability analysis of the uniform mode for antiferromagnetic chains with on-site easy-axis anisotropy described in (I) to include the effect of a shape-dependent demagnetization factor. The purpose has been to explore the influence of the effective spectral gap in the linear dispersion curve at $q=0$ on the modulational instability properties of the nonlinear system and hence on the production properties of ILM's. Linear stability analysis has been used to identify the instability regimes for different values of the demagnetizing factor β, and three qualitatively different signatures have been established. These analytical results, which can only be valid at short times, are shown to connect in a general way with the corresponding long-time evolution of the system as determined by MD simulations. The findings are as follows: (i) For $\beta=0$, the most unstable wave number Q in the modulational instability regime determines the spacing of the incipient and nearly stationary ILM lattice. (ii) For $\beta<0$, the resulting gap in the spin-wave spectrum produces a spin-deviation instability threshold. The larger this gap, the larger the energy that can be stored in the uniform mode before the instability takes hold. MD simulations show that for an energy gap, ILM production is extremely fast at the particular nucleation site and so much energy is drawn from the rest of the lattice that both energetic ILM's and even more energetic point defects consisting of dynamic localized spin flops are formed. These strongly

localized excitations are pinned by the lattice discreteness and remain nearly stationary. (iii) For $\beta>0$, the uniform mode is unstable only to the degenerate $q\neq 0$ spin waves. These in turn are also unstable and drive higher-order instabilities, which ultimately lead to moving ILM's. As these grow in amplitude, become narrower, and decelerate they oscillate at lower frequencies. Interestingly, although ILM's form in all three regimes, the long-time behavior in each case looks qualitatively different. This study shows that many of these differences are a straightforward consequence of variations in the modulational instability process already present at short times.

ACKNOWLEDGMENTS

Discussions with B. Hubbard are appreciated. This work was supported by Grant No. NSF-DMR-9979483.

APPENDIX: MODULATIONAL STABILITY ANALYSIS

1. Nonlinear uniform mode

The stability analysis for the uniform mode described in Refs. 21 and 26 is modified by the presence of sample shape as represented by the Hamiltonian in Eq. (1). The analysis below assumes both $\gamma=1$ and $\hbar=1$. Since the interest is in the stability of the uniform mode (the antiferromagnetic resonance), the sublattice amplitudes can be written as

$$\begin{cases} s_{2n}^{+}(t)=fe^{-i\omega t}; & s_{2n}^{z}=\sqrt{1-f^2}, \\ s_{2n+1}^{+}(t)=ge^{-i\omega t}; & s_{2n+1}^{z}=-\sqrt{1-g^2}. \end{cases} \tag{A1}$$

Substituting these into Eq. (5) yields the two-coupled nonlinear equations

$$\begin{cases} f\Omega=2(1-2\beta)f(1-g^2)^{1/2} \\ \qquad +[(A+3\beta)f+(2+\beta)g](1-f^2)^{1/2}, \\ g\Omega=-2(1-2\beta)g(1-f^2)^{1/2} \\ \qquad -[(A+3\beta)g+(2+\beta)f](1-g^2)^{1/2}, \end{cases} \tag{A2}$$

where the dimensionless frequency $\Omega=\omega/2JS$, the anisotropy parameter $A=D/J$, and the shape parameter β are defined in Eq. (6). Eliminating Ω from Eq. (A2) gives $\alpha=-g/f$ since f and g cannot be chosen independently. α is determined by solving

$$[2+A-2\alpha^{-1}+\beta(1-\alpha^{-1})](1-\alpha^2f^2)^{1/2} +[2+A-2\alpha+\beta(1-\alpha)](1-f^2)^{1/2}=0. \tag{A3}$$

Equation (A3) reveals that α will depend not only on f and A as in (I), but now also on the shape parameter β. From Eqs. (A2) and (A3), the AFMR frequency is

$$\Omega(f)=2(1-\alpha^2f^2)^{1/2}+(A-2\alpha)(1-f^2)^{1/2}+\beta(1-\alpha) \times(1-f^2)^{1/2}-2\beta[(1-\alpha^2f^2)^{1/2}-(1-f^2)^{1/2}] \tag{A4}$$

Note that the first two terms of Eq. (A4) correspond to Eq. (8) of (I), while the last two terms represent the effect of the demagnetization field. Equation (A4) in the limit $f^2\ll 1$ goes over to the more familiar expression for the AFMR frequency,[29,33] namely,

$$\frac{\omega(0)}{2JS}=\sqrt{A(A+4+2\beta)}. \tag{A5}$$

For $q\neq 0$, the last two terms of Eq. (5) vanish, these frequencies do not depend on sample shape, and the result is the same as in (I):

$$\frac{\omega(q\neq 0)}{2JS}=[(A+2)^2-4\cos^2(qa)]^{1/2}. \tag{A6}$$

2. Perturbation analysis of the uniform mode

To investigate the modulational instability of the uniform mode the perturbed spin amplitudes are written in the following general form:

$$\begin{cases} s_{2n}^{+}(t)=(f+b_{2n}+i\Psi_{2n})e^{-i\omega t}; \\ s_{2n}^{z}=(1-f^2)^{1/2}-\left[\dfrac{f}{(1-f^2)^{1/2}}\right]b_{2n}, \\ s_{2n+1}^{+}(t)=(g+b_{2n+1}+i\Psi_{2n+1})e^{-i\omega t}; \\ s_{2n+1}^{z}=-(1-g^2)^{1/2}+\left[\dfrac{g}{(1-g^2)^{1/2}}\right]b_{2n+1}, \end{cases} \tag{A7}$$

where f, g, and $\omega=2JS\Omega$ are related by Eqs. (A3) and (A4), the perturbations $\{b_n\}$ and $\{\Psi_n\}$ are real functions of time, and only the linear terms in the perturbation variables are retained.

Requiring that this perturbed uniform mode again be a solution to the equations of motion, we insert Eq. (A7) into Eq. (5) and obtain the evolution equations for the perturbation variables b_{2n}, b_{2n+1}, Ψ_{2n}, and Ψ_{2n+1}. Expanding these variables in terms of their Fourier components gives

$$\begin{pmatrix} b_{2n} \\ \Psi_{2n} \end{pmatrix}=\sum_Q \begin{pmatrix} b_0(Q) \\ \Psi_0(Q) \end{pmatrix}e^{i(2nQa-\omega_m t)}, \tag{A8}$$

$$\begin{pmatrix} b_{2n+1} \\ \Psi_{2n+1} \end{pmatrix}=\sum_Q \begin{pmatrix} b_1(Q) \\ \Psi_1(Q) \end{pmatrix}e^{i[(2n+1)Qa-\omega_m t]}, \tag{A9}$$

where Q is the modulation wave vector. The resulting equations of motion are

$$\frac{d}{dt}\begin{pmatrix} b_0(Q) \\ b_1(Q) \\ \Psi_0(Q) \\ \Psi_1(Q) \end{pmatrix}=2JS\begin{pmatrix} 0 & T_{12} \\ T_{21} & 0 \end{pmatrix}\begin{pmatrix} b_0(Q) \\ b_1(Q) \\ \Psi_0(Q) \\ \Psi_1(Q) \end{pmatrix} \tag{A10}$$

with

$$T_{12}=\begin{Bmatrix} [(2+\beta)\alpha-\beta](1-f^2)^{1/2} & 2\cos(Qa)(1-f^2)^{1/2} \\ -2\cos(Qa)(1-g^2)^{1/2} & -\left(\frac{2+\beta}{\alpha}-\beta\right)(1-g^2)^{1/2} \end{Bmatrix} \tag{A11}$$

and

$$T_{21}=\begin{Bmatrix} [A+\beta-\alpha(2+\beta)]\frac{f^2}{(1-f^2)^{1/2}} & 2\frac{fg}{(1-g^2)^{1/2}}\cos(Qa) \\ -2\frac{fg}{(1-f^2)^{1/2}}\cos(Qa) & -\left[A+\beta-\frac{2+\beta}{\alpha}\right]\frac{g^2}{(1-g^2)^{1/2}} \end{Bmatrix} -T_{12}. \tag{A12}$$

Note that upon setting $\beta=0$ in Eqs. (A11) and (A12), Eqs. (6.9)–(6.13) of Ref. 26 are recovered. Incidentally, the matrices (A11) and (A12) have to be augmented by another term for $Q=0$. This reflects the fact that spatially uniform perturbations do not modulate the uniform mode, but simply tune its amplitude and phase. Thus the form of the equations for $Q=0$ does not coincide with that for all other Q values.

We are now in a position to determine the stability of the uniform mode of amplitude f relative to spin-wave modulation of wave number Q as a function of the shape parameter β. Equation (A10) becomes an eigenvector equation with nontrivial solutions only when

$$\det|\lambda\vec{\vec{I}}-i\vec{\vec{T}}|=0, \tag{A13}$$

where a normalized modulation frequency $\lambda=\omega_m/2JS$ is introduced. This is the stability parameter defined in Eq. (7). Due to the vanishing diagonal entries of $\vec{\vec{T}}$, Eq. (A13) simplifies to

$$\det|\lambda^2\vec{\vec{I}}+T_{21}T_{12}|=0. \tag{A14}$$

The real part of λ represents a frequency shift relative to the uniform mode Ω, and the imaginary part of λ determines the amplitude growth rate of the modulation of wave number Q. If λ is real for all Q, no instability occurs.

Solving Eq. (A13) for λ yields

$$\lambda^2=(\alpha C+B\alpha^{-1})-4E\sin^2(Qa)-[(\alpha C+B\alpha^{-1})^2-F -4(BC+G)\sin^2(Qa)]^{1/2}, \tag{A15}$$

where

$$B=-\left[\frac{1}{2}(2+\beta-\beta\alpha^{-1})A+2\right]g^2-2\alpha[(1-f^2)(1-g^2)]^{1/2} +\frac{\alpha^{-1}}{2}(2+\beta)^2-\beta(\beta+2)+\frac{1}{2}\alpha\beta^2, \tag{A16a}$$

$$C=-\left[\frac{1}{2}(2+\beta-\alpha\beta)A+2\right]f^2-2\alpha^{-1}[(1-f^2)(1-g^2)]^{1/2} +\frac{\alpha}{2}(2+\beta)^2-\beta(\beta+2)+\frac{\alpha^{-1}\beta^2}{2}, \tag{A16b}$$

$$E=gf-[(1-f^2)(1-g^2)]^{1/2}, \tag{A16c}$$

$$F=\beta(2+\beta)(\alpha^{-1}+\alpha-2) \times[\beta(2+\beta)(\alpha^{-1}+\alpha-2)-A(2+\beta)(\alpha^{-2}+\alpha^2)fg -A\beta(f^2+g^2)-A^2(fg)^2+4(E^2-1)], \tag{A16d}$$

and

$$G=\frac{1}{4}(1-\alpha^{-1})^2\beta(\beta+2)\times(-(\alpha-1)^2\beta(\beta+2+Afg) +4(A+1)(\alpha^{-1}+\alpha)g^2+\alpha(A^2-8)(fg)^2 +4g^2\{A-2[(1-f^2)(1-g^2)]^{1/2}\}). \tag{A16e}$$

Note that both F and G vanish for $\beta=0$, so that Eq. (A14) contains Eq. (19) of (I) as a special case. In the small-amplitude limit,

$$F+4G\sin^2(Qa)=[(\alpha-1)^2\alpha^{-1}\beta(\beta+2)]^2[1-\sin^2(Qa)] \geqslant 0, \tag{A17}$$

which ensures that the linear solutions for any value of β are real. Furthermore, in the limit of $Q\to 0$, Eq. (A15) reduces to

$$\lambda^2=(\alpha C+B\alpha^{-1})-[(\alpha C+B\alpha^{-1})^2-F]^{1/2}, \tag{A18}$$

which is strictly positive for $\beta\neq 0$. Thus, the factor F is responsible for the discontinuity of the dispersion curve at $Q=0$ for nonzero β.

[1] A. J. Sievers and S. Takeno, Phys. Rev. Lett. **61**, 970 (1988).
[2] R. S. MacKay and S. Aubry, Nonlinearity **7**, 1623 (1994).
[3] A. J. Sievers and J. B. Page, in *Dynamical Properties of Solids*, edited by G. K. Horton and A. A. Maradudin (North-Holland, Amsterdam, 1995), Vol. 7, p. 137.
[4] S. Flach and C. R. Willis, Phys. Rep. **295**, 181 (1998).

[5] M. Peyrard, Physica D **119**, 184 (1998).
[6] A. R. Bishop and T. Schneider, in *Springer Series in Solid-State Sciences*, edited by M. Cardona, P. Fulde, and H.-J. Queisser (Springer-Verlag, Berlin, 1978).
[7] A. R. Bishop, D. K. Campbell, P. Kumar, and S. E. Trullinger, in *Springer Series in Solid-State Sciences*, edited by M. Cardona, P. Fulde, K. v. Klitzing, and H.-J. Queisser (Springer-Verlag, Berlin, 1987), Vol. 69.
[8] P. M. Chaikin and T. C. Lubensky, *Principles of Condensed Matter Physics* (Cambridge University, Cambridge, England, 1995), Chap. 10.
[9] Y. S. Kivshar and M. Peyrard, Phys. Rev. A **46**, 3198 (1992).
[10] T. Dauxois and M. Peyrard, Phys. Rev. Lett. **70**, 3935 (1993).
[11] K. W. Sandusky and J. B. Page, Phys. Rev. B **50**, 866 (1994).
[12] I. Daumont, T. Dauxois, and M. Peyrard, Nonlinearity **10**, 617 (1997).
[13] T. Rössler and J. B. Page, Phys. Rev. Lett. **78**, 1287 (1997).
[14] T. Rössler and J. B. Page, Phys. Rev. B **62**, 11 460 (2000).
[15] C. W. Hass and H. B. Callen, in *Magnetism*, edited by G. T. Rado and H. Suhl (Academic, New York, 1963), Vol. I, p. 449.
[16] H. Suhl, J. Phys. Chem. Solids **1**, 209 (1957).
[17] H. Suhl, J. Appl. Phys. **29**, 416 (1958).
[18] A. J. Heeger and P. Pincus, Phys. Rev. Lett. **10**, 53 (1963).
[19] R. W. Damon, in *Magnetism*, edited by G. T. Rado and H. Suhl (Academic, New York, 1963), Vol. I, p. 552.
[20] M. Sparks, *Ferromagnetic Relaxation Theory* (McGraw-Hill, New York, 1964), p. 24.
[21] R. Lai and A. J. Sievers, Phys. Rev. B **57**, 3433 (1998).
[22] R. Lai and A. J. Sievers, Phys. Rev. Lett. **81**, 1937 (1998).
[23] U. T. Schwarz, L. Q. English, and A. J. Sievers, Phys. Rev. Lett. **83**, 223 (1999).
[24] L. Q. English, M. Sato, and A. J. Sievers, J. Appl. Phys. **89**, 6707 (2001).
[25] M. Sato, L. Q. English, B. E. Hubbard, and A. J. Sievers, J. Appl. Phys. **91**, 8676 (2002).
[26] R. Lai and A. J. Sievers, Phys. Rep. **314**, 147 (1999).
[27] F. Keffer and C. Kittel, Phys. Rev. **85**, 329 (1952).
[28] F. Keffer, in *Handbuch der Physik*, edited by H. P. J. Wijn (Springer-Verlag, Berlin, 1966), Vol. XVIII/2.
[29] M. Chikamatsu, M. Tanaka, and H. Yamazaki, J. Phys. Soc. Jpn. **50**, 2876 (1981).
[30] M. C. Cross and P. C. Hohenberg, Rev. Mod. Phys. **65**, 851 (1993).
[31] A. G. Gurevich and G. A. Melkov, *Magnetization Oscillation and Waves* (CRC, New York, 1996), p. 69.
[32] S. R. Bickham, A. J. Sievers, and S. Takeno, Phys. Rev. B **45**, 10 344 (1992).
[33] A. H. Morrish, *The Physical Principles of Magnetism* (Wiley, New York, 1965), p. 623.